

Finite-size Domains in a Membrane with Two-state Active Inclusions

Chien-Hsun Chen

Department of Physics and Center for Complex Systems, National Central University, Jhongli 32054, Taiwan

Abstract

We propose a model that leads to the formation of non-equilibrium finite-size domains in a biological membrane. Our model considers the active conformational change of the inclusions and the coupling between inclusion density and membrane curvature. Two special cases with different interactions are studied by Monte Carlo simulations. In case (i) excited state inclusions prefer to aggregate. In case (ii) ground state inclusions prefer to aggregate. When the inclusion density is not coupled to the local membrane curvature, in case (i) the typical length scale (\sqrt{M}) of the inclusion clusters shows weak dependence on the excitation rate (K_{on}) of the inclusions for a wide range of K_{on} but increases fast when K_{on} becomes sufficiently large; in case (ii) $\sqrt{M} \sim K_{on}^{-\frac{1}{3}}$ for a wide range of K_{on} . When the inclusion density is coupled to the local membrane curvature, the curvature coupling provides the upper limit of the inclusion clusters. In case (i) (case (ii)), the formation of the inclusions is suppressed when K_{off} (K_{on}) is sufficiently large such that the ground state (excited state) inclusions do not have sufficient time to aggregate. We also find that the mobility of an inclusion in the membrane depends on inclusion-curvature coupling. Our study suggests possible mechanisms that produce finite-size domains in biological membranes.

Acknowledgement

This work is supported by the National Science Council of the Republic of China under grant no. NSC 92-2112-M-008-019, NSC 93-2112-M-008-030, and NSC 94-2112-M-008-020. This thesis is submitted to the Department of Physics, National Central University by Chien-Hsun Chen in partial fulfillment of the requirements for the Master degree in Physics. The author would like to thank Prof. Hsuan-Yi Chen for supervising this work, and Mr. Jia-Yuan Wu and Yong-Hsiang Chen for stimulating discussions.

Contents

1	Introduction	1
2	The model	4
2.1	Introduction	4
2.2	The Hamiltonian	6
3	Simulation method	11
3.1	Metropolis algorithm	11
3.2	Monte Carlo step	13
3.3	Statistics of cluster size	15
4	Simulation results and discussion	21
4.1	Cluster size distribution	21
4.2	Simulation results	22
4.2.1	Short-time in-plane motions of inclusions	26
4.2.2	Case 1	31
4.2.3	Case 2	35

5	Summary	39
A	Non-dimensionalization of the Hamiltonian	43

Chapter 1

Introduction

As shown in Figure 1.1, a biological membrane is a self-assembled bilayer composed of various types of macromolecules such as lipids, proteins, carbohydrates, cholesterol, and other materials. [1] A membrane is thought to be similar to a two-dimensional fluid, therefore the aforementioned molecules can diffuse on it. Many experimental and theoretical studies have shown that the distribution of these molecules in a membrane is nonuniform. [2] Instead, some molecules aggregate to form domains with typical length scale ranging from tens of nanometers to about one micrometer. [3] An important subject of current biomembrane research is to find the mechanisms that is responsible for the formation of these finite-size domains. From equilibrium statistical mechanism, we know that if there are only short-range interactions between the molecules, equilibrium macrophase separation can be induced in a system, but equilibrium microphase separation can not be induced if there are no long-range interactions in a system. However, up to now there has been no clear evidence for such long-range interactions in the membrane. Several possible mechanisms for the

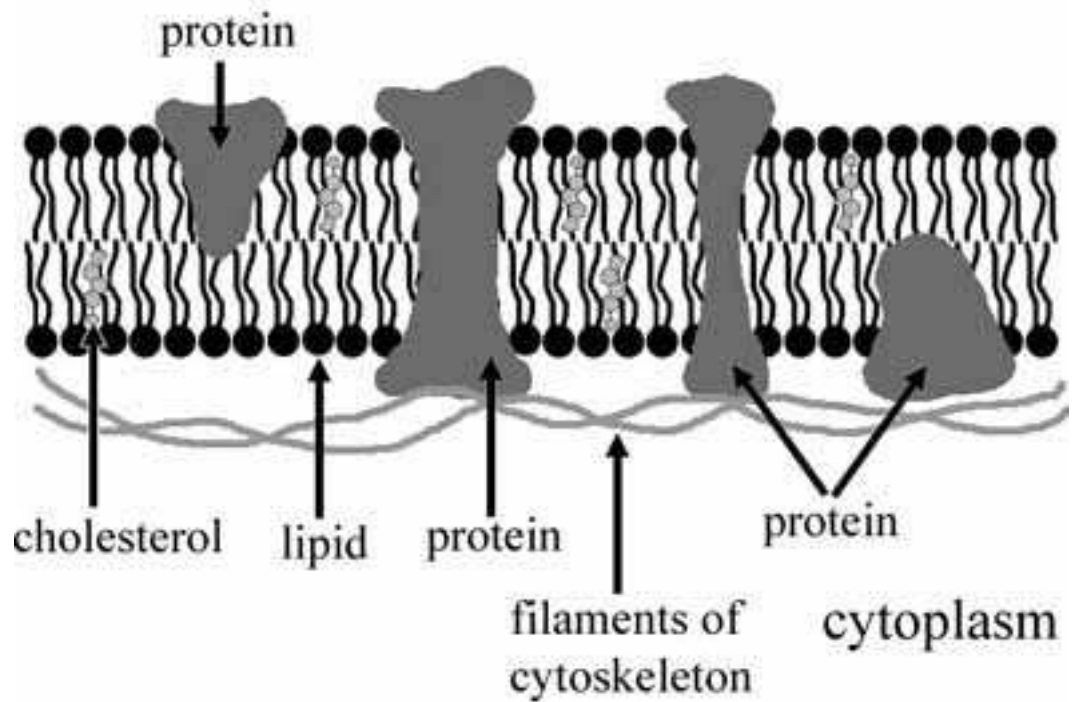


Figure 1.1: The configuration of membrane is shown in this figure.

formation of finite-size domains in biological membranes have been proposed, including (i) the kinetics of spontaneous membrane domain assembly depends on the effect of membrane recycling ubiquitous in the living cells [4, 5], (ii) cholesterol can induce separate domains of two mixed fatty acids [6, 7]. Although the true mechanisms of raft formation has not been verified yet, it is possible that different mechanisms are involved in different situations.

Since the activities of proteins in the membranes are important in many physiological processes including ion transport, signal transduction, et al., in this thesis we propose that the activities of proteins can also lead to the formation of finite-size

domains in the membranes. To concentrate on the basic mechanism behind activity-induced finite-size domains, in our model the system contains only one type of lipids and one type of active proteins. These proteins are called inclusions in this thesis. The inclusions can change their internal states, and different internal states of inclusions have different conformations and different interaction with other molecules. Therefore this work is a natural extension of Ref [8], in which the fluctuation spectrum and the stability of the homogeneous state in such systems were studied. Monte Carlo simulation is applied to illustrate our proposal. From the result of simulation, we find that: (1) The distribution of inclusions in a membrane can be controlled by the rate of conformational change of the inclusions. (2) The coupling between inclusion density and membrane curvature provides the upper limit of the typical size of the inclusion clusters. (3) The mobility of inclusions in the membrane depends on inclusion-curvature coupling.

This thesis is organized as follows. In chapter 2 we introduce the model and the Hamiltonian of our system. Chapter 3 discusses the simulation algorithm. Chapter 4 analyzes the result of simulation. Chapter 5 summarizes this thesis.

Chapter 2

The model

2.1 Introduction

Since we propose that the formation of heterogeneous structure in biological membranes can be controlled by the activities (i.e., conformational changes) of the membrane inclusions, to illustrate our proposal we consider a model in which the membrane is composed of only one type of lipid molecules and one type of active inclusions with two conformational states. These inclusions change their conformational states by either external energy drive (ATP, light, etc.), or by ligands. Therefore the membrane is called an active membrane. Schematics of the conformations of an inclusion and its surrounding lipids is shown in Figure 2.1. Different conformations of an inclusion prefer different local membrane curvature, thus the inclusions also induce local membrane curvature. We discuss the Hamiltonian that describes our model in the following section.

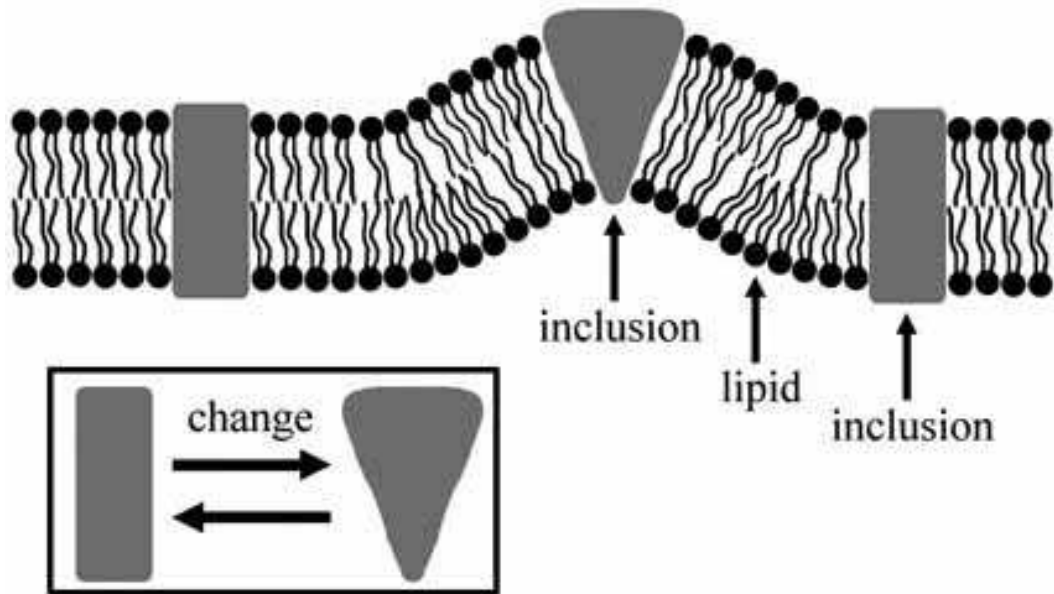


Figure 2.1: Schematics of two conformations of an inclusion and its surrounding lipids. Different states of an inclusion have different conformation, thus they induce different local membrane curvature.

2.2 The Hamiltonian

Our simulation is carried out on a lattice model. In our model, the configuration of the system is described by two scalar fields h and n . As shown in Figure 2.2, h and n are defined on a square lattice with lattice constant a . The size of a is chosen to be the smallest length scale beyond which the continuum elastic description of membranes breaks down ($a \approx 5nm$). [9] h_{ij} is the height of the membrane measured from a reference plane (xy -plane) at lattice patch (i, j) , and n_{ij} denotes what molecule is at patch (i, j) and is defined in the following way,

$$n_{ij} = \begin{cases} 0 & , \text{ if patch } (i, j) \text{ is occupied by lipids,} \\ 1 & , \text{ if patch } (i, j) \text{ is occupied by an inclusion in ground state,} \\ 2 & , \text{ if patch } (i, j) \text{ is occupied by an inclusion in excited state.} \end{cases} \quad (2.1)$$

The lipids and inclusions are allowed to move in the membrane and the inclusions can change their conformations.

The Hamiltonian of the membrane includes: (1) the bending energy of the membrane, (2) the surface tension of the membrane, (3) the coupling between inclusion density and membrane curvature, and (4) the interaction energy between the inclusions and lipid molecules. Therefore the discretized form of the hamiltonian of the membrane that includes all the above terms can be written as

$$\begin{aligned} H_{lattice} = & \sum_{(i,j)} \frac{a^2}{2} \left[\kappa (\nabla_{\perp}^2 h)_{ij}^2 + \gamma (|\nabla_{\perp} h|^2)_{ij} \right] \\ & - \sum_{(i,j)} \sum_{p=0}^2 a^2 \kappa C_p \phi_p(i, j) (\nabla_{\perp}^2 h)_{ij} \\ & + \frac{1}{2} \sum_{\langle\langle i,j \rangle\rangle \langle\langle k,l \rangle\rangle} \left(\sum_{m,n} J_{mn} \phi_m(i, j) \phi_n(k, l) \right), \end{aligned} \quad (2.2)$$

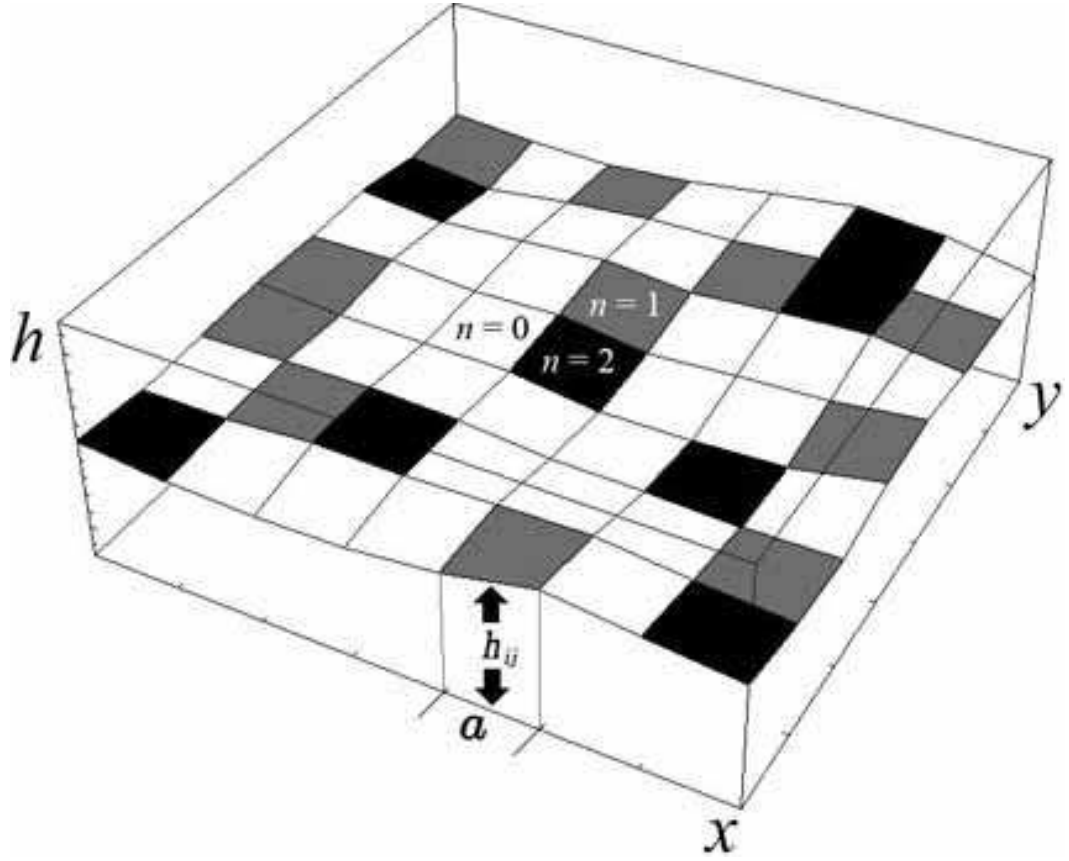


Figure 2.2: The configuration of the system is described by h and n . The reference plane is discretized into a square lattice with lattice constant $a \sim 5nm$, and $h_{i,j}$ is the height of the membrane measured from a flat reference plane at patch (i, j) . A white patch is occupied by lipids, and $n = 0$ at this patch. A gray patch is occupied by a ground state inclusion ($n_{ij} = 1$ at this patch). A black patch is occupied by an excited state inclusion ($n_{ij} = 2$ at this patch).

where κ is the membrane bending rigidity constant, and γ is the surface tension constant of the membrane, C_p is curvature-inclusion coupling of type- p component, and the last term on the right hand side of Eq. (2.2) is the short range interaction between the patches, thus J_{mn} is the interaction energy between one type- m patch and a nearest neighboring type- n patch. The short-range interactions between the molecules in the membrane could be induced by hydrophobic length mismatch or other short range interactions. [10] As shown in Figure 2.3, when the hydrophobic length of the inclusions is different from that of a lipid bilayer, the lipid bilayer is stretched or compressed from its relaxed thickness. Then free energy of the system is increased due to this inclusion-induced thickness variation. Therefore the inclusions aggregate together to lower the free energy of the system. Besides the hydrophobic length mismatch effect, other short-range interactions between the inclusions also exist. $\sum_{(i,j)}$ means sum over all patches, and $\sum_{\langle(i,j)(k,l)\rangle}$ means sum over all nearest neighboring pairs. ϕ_m is defined as follows:

$$\left\{ \begin{array}{l} \text{if } n_{ij} = 0, \text{ then } \phi_0(i, j) = 1, \phi_1(i, j) = \phi_2(i, j) = 0, \\ \text{if } n_{ij} = 1, \text{ then } \phi_1(i, j) = 1, \phi_0(i, j) = \phi_2(i, j) = 0, \\ \text{if } n_{ij} = 2, \text{ then } \phi_2(i, j) = 1, \phi_0(i, j) = \phi_1(i, j) = 0. \end{array} \right. \quad (2.3)$$

The discretized bending energy and surface energy are

$$\sum_{(i,j)} \frac{a^2 \kappa}{2} (\nabla_{\perp}^2 h)_{ij}^2 = \sum_{(i,j)} \frac{a^2 \kappa}{2} \left(\frac{h_{i+1,j} + h_{i-1,j} - 4h_{i,j} + h_{i,j+1} + h_{i,j-1}}{a^2} \right)^2, \quad (2.4)$$

and

$$\sum_{(i,j)} \frac{a^2 \gamma}{2} (|\nabla_{\perp} h|^2)_{ij} = \sum_{(i,j)} \frac{a^2 \gamma}{2} \left| \left(\frac{h_{i+1,j} - h_{i-1,j}}{2a} \right) \hat{i} + \left(\frac{h_{i,j+1} - h_{i,j-1}}{2a} \right) \hat{j} \right|^2. \quad (2.5)$$

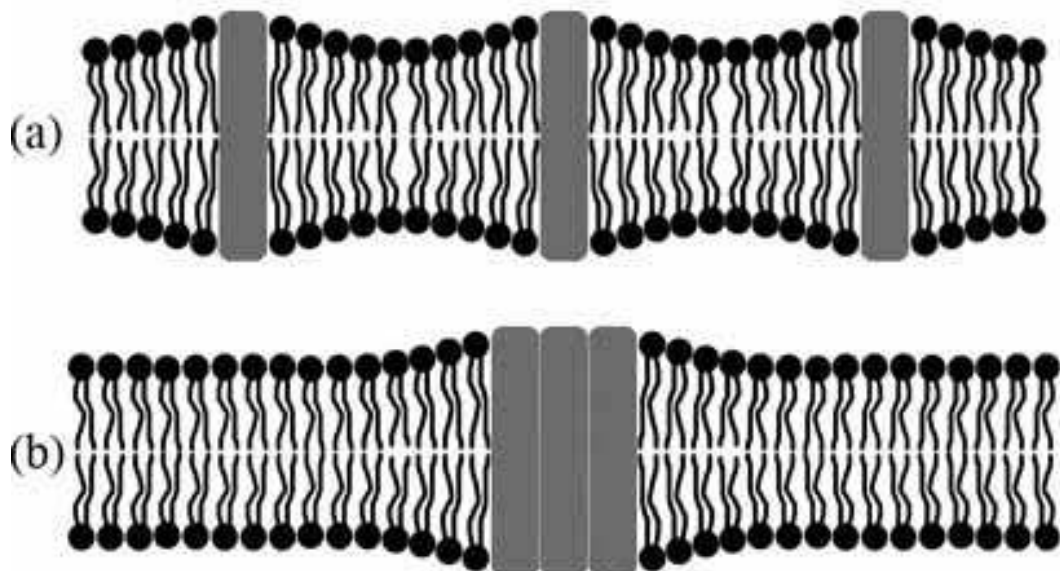


Figure 2.3: Inclusion-inclusion attraction can be induced by hydrophobic mismatch. When the hydrophobic length of the inclusions is different from that of a lipid bilayer, the lipid bilayer is stretched or compressed from its relaxed thickness. Then free energy of the system is increased due to this inclusion-induced thickness variation. Inclusions could aggregate together to lower the free energy of the system. Free energy of (b) is lower than (a).

Symbol	Typical Value
κ	$\sim 5 \times 10^{-20} N \cdot m$ [11]
γ	$\sim 24 \times 10^{-6} N/m$ [12]
a	$\sim 5nm$ [9]
h_0	$\sim 1nm$
C_p	$\sim 1/nm$
J_{mn}	$\sim 1 - 10k_B T$

Table 2.1: Typical values of the parameters.

Typical values of κ , γ , a , h_0 , C_p , and J_{mn} are listed in Table 2.1. For convenience the non-dimensionalized hamiltonian is introduced. The unit energy is $k_B T$, the unit length in the xy -plane is a , and the unit length in the z -direction is $h_0 \equiv a\sqrt{\frac{k_B T}{\kappa}}$.

Therefore, the non-dimensionalized hamiltonian is

$$\begin{aligned}
\tilde{H}_{lattice} = & \sum_{(i,j)} \frac{1}{2} \left[\left(\tilde{\nabla}_{\perp}^2 \tilde{h} \right)_{ij}^2 + \frac{\gamma a^2}{\kappa} \left(\left| \tilde{\nabla}_{\perp} \tilde{h} \right|^2 \right)_{ij} \right] \\
& - \sum_{(i,j)} \sum_{p=0}^2 G_p \phi_p(i, j) \left(\tilde{\nabla}_{\perp}^2 \tilde{h} \right)_{ij} \\
& + \frac{1}{2} \sum_{\langle\langle i,j \rangle\rangle \langle\langle k,l \rangle\rangle} \left(\sum_{m,n} \tilde{J}_{mn} \phi_m(i, j) \phi_n(k, l) \right), \tag{2.6}
\end{aligned}$$

where $G_p \equiv h_0 C_p$ is the non-dimensionalized inclusion-curvature coupling, $\tilde{h}_{ij} \equiv \frac{1}{h_0} h_{ij}$, $\tilde{J}_{mn} \equiv \frac{1}{k_B T} J_{mn}$, $\tilde{\nabla}_{\perp} \equiv \frac{1}{a} \nabla_{\perp}$, and $\tilde{\nabla}_{\perp}^2 \equiv \frac{1}{a^2} \nabla_{\perp}^2$.

Chapter 3

Simulation method

Monte Carlo simulation is applied to study the model we introduced in the previous chapter. In our simulation, one Monte Carlo step has three parts: (1) The in-plane motion of materials in the membrane is simulated by Kawasaki exchange dynamics. [13] (2) The dynamics of membrane height is simulated by Metropolis algorithm. (3) The excitation/relaxation of the inclusions are introduced in the simulation by assigning each inclusion certain probability to change its state in each Monte Carlo step. When the system has reached the steady state, Hoshen-Kopelman algorithm is applied to analyze the size distribution of inclusion clusters in the system.

3.1 Metropolis algorithm

Metropolis algorithm provides a set of rules to update the microscopic state of a system such that in the long time limit the probability that the system is in a microscopic state approaches the equilibrium distribution. For example, consider a system

described by a single variable x and equilibrium distribution $\omega(x)$. Let us assume the system to be at state x_n at some instance, we first choose a trial step to change state from x_n to x_t . Let

$$\gamma = \omega(x_t)/\omega(x_n), \quad (3.1)$$

if $\gamma \geq 1$, then the trial step is accepted and the new state of the system become x_t . On the other hand, if $\gamma < 1$, then the trial step has probability γ to be accepted. If the trial step is rejected, then the system remains at state x_n . In the following we prove that in the long time limit the probability that the system is in state x is given by $\omega(x)$. [13, 14] For an ensemble of independent systems of random initial conditions, let $P_n(x)$ be the probability for a system to be in state x at the n -th step, and the net probability for a system changing from state x to state y in the next step is

$$\begin{aligned} \Delta P(x \rightarrow y) &= P_n(x)P(x \rightarrow y) - P_n(y)P(y \rightarrow x) \\ &= P_n(y)P(x \rightarrow y) \left[\frac{P_n(x)}{P_n(y)} - \frac{P(y \rightarrow x)}{P(x \rightarrow y)} \right]. \end{aligned} \quad (3.2)$$

Where $P(x \rightarrow y)$ is the probability for a system to change its state from x to y in a step. When

$$\frac{P_n(x)}{P_n(y)} = \frac{P_e(x)}{P_e(y)} \equiv \frac{P(y \rightarrow x)}{P(x \rightarrow y)}, \quad (3.3)$$

the system is in equilibrium. From equation (3.2), it is clear that if $\frac{P_n(x)}{P_n(y)} > \frac{P_e(x)}{P_e(y)}$, then $\Delta P(x \rightarrow y) > 0$. On the other hand, when $\frac{P_n(x)}{P_n(y)} < \frac{P_e(x)}{P_e(y)}$ then $\Delta P(x \rightarrow y) < 0$.

Thus,

$$\lim_{n \rightarrow \infty} \frac{P_n(x)}{P_n(y)} \rightarrow \frac{P_e(x)}{P_e(y)}. \quad (3.4)$$

In the Metropolis algorithm,

$$P(x \rightarrow y) = T(x \rightarrow y)A(x \rightarrow y), \quad (3.5)$$

where $T(x \rightarrow y)$ is the probability for a trial step from state x to state y to be chosen, $A(x \rightarrow y)$ is the probability for this trial step to be accepted. In the simulation the trial steps are chosen such that $T(x \rightarrow y) = T(y \rightarrow x)$, therefore

$$\frac{N_e(x)}{N_e(y)} = \frac{A(y \rightarrow x)}{A(x \rightarrow y)}. \quad (3.6)$$

In Metropolis algorithm, if $\omega(x) > \omega(y)$, then $A(y \rightarrow x) = 1$ and $A(x \rightarrow y) = \frac{\omega(y)}{\omega(x)}$.

If $\omega(x) < \omega(y)$, then $A(y \rightarrow x) = \frac{\omega(y)}{\omega(x)}$ and $A(x \rightarrow y) = 1$. This leads to

$$\frac{N_e(x)}{N_e(y)} = \frac{\omega(x)}{\omega(y)}. \quad (3.7)$$

That is, in the long time limit the probability distribution of the system reaches $\omega(x)$.

3.2 Monte Carlo step

In our simulation, each Monte Carlo step has 3 parts. The first part is Kawasaki exchange dynamics for the materials in the membrane. We choose one patch randomly, and exchange the material on it with a randomly chosen nearest neighbor patch with Metropolis rule. From kawasaki exchange dynamics, time scale of one Monte Carlo step can be estimated in the following way. The dimension of diffusion constant is

$$[D] = \frac{L^2}{T}. \quad (3.8)$$

For typical macromolecules diffusing in a membrane, $D \sim 1\mu m^2/s$ [15]. In the absence of any interactions, these materials in the membrane move a distance $a \sim 5nm$ per

Monte Carlo step, therefore each Monte Carlo step corresponds to a time interval $\Delta t \sim a^2/4D \sim 10^{-5}s$. In the second part, we choose a new patch at random, and update the membrane height at this patch by $\Delta h \times \text{ran}(-1, 1)$ with Metropolis algorithm, where Δh is chosen to be $\sim 0.4nm$, and $\text{ran}(-1, 1)$ is a random number between -1 and 1. In the third part, we choose an inclusion randomly, and allow the inclusion to change its conformation in the following way: if the inclusion is in the ground (excited) state, then it has probability $K_{on} \cdot \Delta t$ ($K_{off} \cdot \Delta t$) to change its conformation to excited (ground) state, where K_{on} (K_{off}) is the excitation (relaxation) rate. The first and second part are repeated for N_{lat} (total number of patches in the system) times per Monte Carlo step. The third part is chosen such that on average each inclusion has performed one trial conformational change in each Monte Carlo step. Moreover, Metropolis algorithm is applied to the first and the second parts, but in the third part the excitation rate and relaxation rate of inclusions are constant. Therefore the third part drives the system out of equilibrium, and K_{on} , K_{off} are the important time scales which affect the distribution of inclusions.

The size of the system in the simulations is 128×128 to 256×256 patches. Total number of inclusions in this system is

$$N_{inc} = \sum_{(i,j)} (\phi_1 + \phi_2). \quad (3.9)$$

For convenience, we also introduce the average inclusion density $\phi_{inc} \equiv N_{inc}/N$. The simulations begin with $\frac{1}{2}\phi_{inc}N$ ground state inclusions and $\frac{1}{2}\phi_{inc}N$ excited state inclusions dispersed randomly in a flat discretized membrane. Periodic boundary condition is applied in all simulations. After the system has reached steady state, the

simulation is performed with up to 10^7 Monte Carlo steps, and data are taken for every 1000 Monte Carlo steps.

3.3 Statistics of cluster size

After the system has reached steady state, Hoshen-Kopelman algorithm, a very fast and straight method, is applied to analyze the size distribution of inclusion clusters. [13] Figure 3.1 shows an example of a square lattice containing inclusions (gray patches) and lipids (white patches), and the size and number of inclusion clusters are to be determined.

As shown in Figure 3.2, this is done by going through each row of the lattice from left to right, from top to bottom in turn and assigning each gray patch with a number n which we call “cluster index” in the following way. The cluster index begins from 1. When a gray patch has a nearest-neighbor gray patch that has been visited, then the patch is assigned by the same cluster index as this neighbor. On the other hand, when a gray patch has no nearest-neighbor gray patch that has been visited, then we assign a new number ($1 + n_{max}$, where n_{max} is the maximum n that has been assigned up to this patch) to this patch. More than one cluster index can be associated with the visited nearest-neighbors of a gray patch. Figure 3.2-3.5 illustrate some examples. The example in Figure 3.2 is when cluster 1 and cluster 2 are actually the same cluster. In this situation, the Hoshen-Kopelman method corrects such “mislabeling” by introducing another set of variable N_n , which is called “the label of the n^{th} cluster”. If $N_n > 0$, N_n keeps track of the number of patches

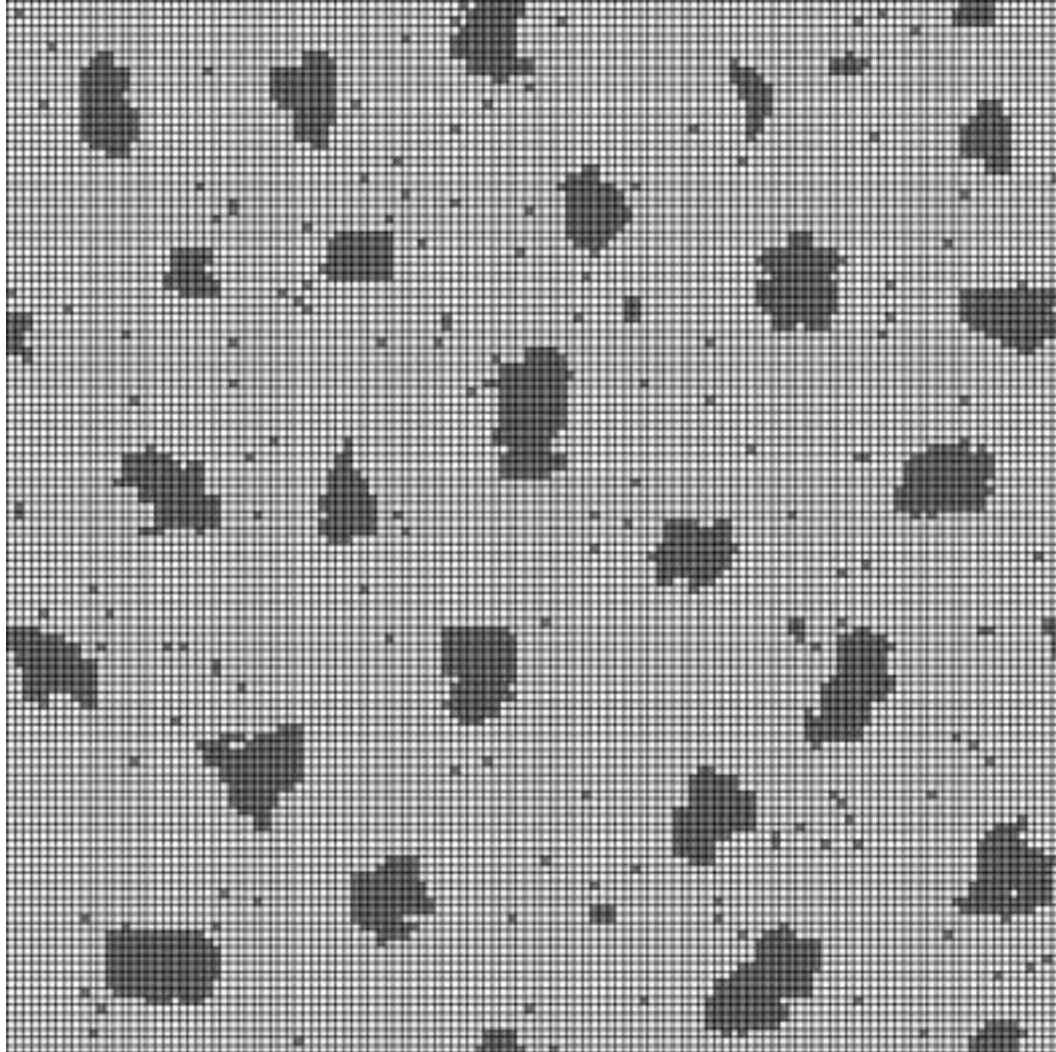


Figure 3.1: A 128×128 square lattice containing inclusions (gray patches) and lipids (white patches).

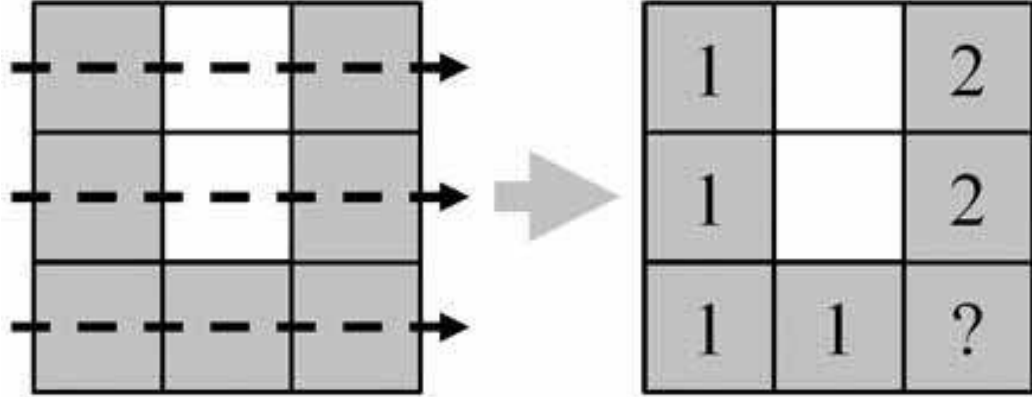


Figure 3.2: Labeling patches on a square lattice. This is done by going through each row of the lattice from left to right, then from top to bottom in turn and assigning each gray patch with a number n (cluster index) in the following way. The cluster index begins from 1. If a gray patch has a nearest-neighbor gray patch that has been visited, then the patch is assigned by the same cluster index as this neighbor. On the other hand, if a gray patch has no nearest-neighbor gray patch that has been visited, then we assign a new number ($1 + n_{max}$, where n_{max} is the maximum n that has been assigned up to this patch) to it. In the third row, more than one cluster indices are associated with the nearest neighbors of a gray patch, therefore cluster 1 and cluster 2 are actually the same cluster.

belong to the n^{th} cluster. If $N_n < 0$, N_n denotes that the n^{th} cluster actually belongs to the cluster labeled by $-N_n$.

The way to determine the cluster index in Figure 3.2 is discussed in Figure 3.3. In Figure 3.4, the n 's and N_n 's of the nearest neighbors of the new gray patch are different, and they belong to different clusters. In Figure 3.5, the n 's and N_n 's of the nearest neighbors of the new gray patch are again different, but they actually belong to the same cluster. Figure 3.4 and 3.5 explain how Hoshen-Kopelman method update both n and N_n . After labeling all patches of the system, we obtain the number of clusters and the distribution of cluster size from the final values of N_n 's.

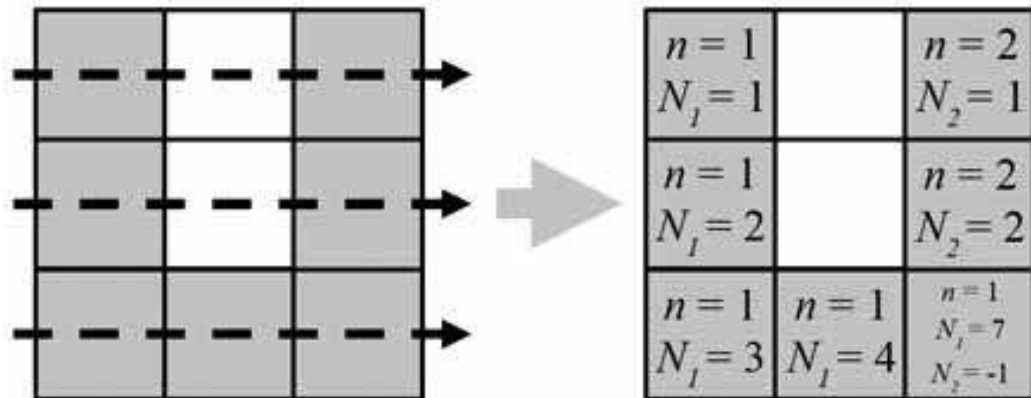


Figure 3.3: Hoshen-Kopelman algorithm introduces new variable N_n , i.e., “the labels of cluster index n ”. If $N_n > 0$, N_n is the number of patches belongs to the cluster labeled by n . If $N_n < 0$, N_n denotes that the cluster labeled by n belongs to the cluster labeled by $-N_n$. In the right corner of the third row, when there are more than one cluster index “ n ” associated with the nearest neighbors of a new gray patch, we check the N_n ’s of those neighbors first. In the figure, N_n of the neighboring labeled patches are all positive ($N_1 = 4$, $N_2 = 2$). Therefore for the new gray patch, $n=1$ (minimum cluster index of the nearest neighbors), and N_1 is replaced by $N_1 + N_2 + 1 = 4 + 2 + 1 = 7$, and N_2 is replaced by -1 , indicating that cluster with label $n = 2$ actually belongs to $n = 1$ cluster.

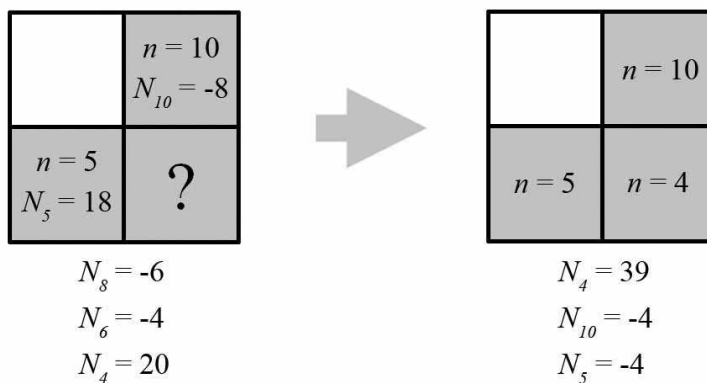


Figure 3.4: In this case, for the patch labeled by “?”, N_n of its neighboring patches are not all positive, $N_{10} = -8$, but $N_8 = -6$, $N_6 = -4$, and $N_4 = 20$. In this case, the index of the new labeled gray patch is labeled by $n = 4$, and N_4 is replaced by $N_4 + N_5 + 1 = 20 + 18 + 1 = 39$. N_{10} and N_5 are both replaced by -4 .

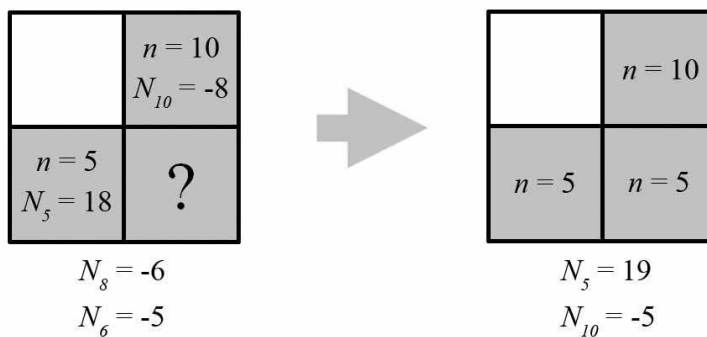


Figure 3.5: In this case, $N_{10} = -8$, $N_8 = -6$, $N_6 = -5$, and $N_5 = 18$, thus the neighbors of the patch labeled by “?” actually belong to the same cluster. The index of this new patch is $n = 5$, and N_5 is replaced by $N_5 + 1 = 18 + 1 = 19$, and N_{10} is replaced by -5 .

Chapter 4

Simulation results and discussion

4.1 Cluster size distribution

The simulations begin with $\frac{1}{2}\phi_{inc}N$ ground state inclusions and $\frac{1}{2}\phi_{inc}N$ excited state inclusions dispersed randomly in a flat discretized membrane. Periodic boundary condition is applied in all simulations. After the system has reached steady state, the simulation is performed with up to 10^7 Monte Carlo steps, and data are taken for every 1000 Monte Carlo steps. The size of all inclusion clusters can be found by the method discussed in Chapter 3. The distribution of inclusion cluster size is defined by

$$P(\omega) = \omega \cdot \left[\frac{n_\omega}{\sum_{\omega=1}^{\infty} (\omega \cdot n_\omega)} \right], \quad (4.1)$$

where $P(\omega)$ is the probability that an inclusion is found in a cluster with ω patches, and n_ω is the total number of clusters with ω patches. Figure 4.1 shows $P(\omega)$ for $\kappa = 5 \times 10^{-20}N \cdot m$, $\gamma = 24 \times 10^{-6}N/m$, $\phi_{inc} = 12.5\%$, $K_{off}\Delta t = 10^{-3}$, $K_{on}/K_{off} = 1/32$,

$\tilde{J}_{01} = \tilde{J}_{12} = \tilde{J}_0 + 1.5$, all other $\tilde{J}_{mn} = \tilde{J}_0$, $G_2 = 0$, $G_1 = 0, -1$, and -2 . The maximum at $\omega = 1$ comes from single-inclusion clusters spreading around in the “inclusion-poor” domains. Another maximum of $P(\omega)$ at greater ω comes from finite-size inclusion clusters, this is the typical size of the inclusion clusters. Figure 4.2 shows typical snapshots for steady state inclusion distribution and membrane morphology for the same parameters as in Figure 4.1. The length scale in the z -direction is chosen to be the same as x and y directions (the unit length is a) in order to faithfully present the morphology of the membrane. One clearly sees that as $|G_1|$ increases the curvature of the membrane in the inclusion-rich domains increases and the typical size of inclusion clusters becomes smaller. Furthermore, when $G_1 \neq 0$ the location of inclusion clusters have strong correlation with the regions with high local membrane curvature. This is because the system has lower free energy when the inclusions locate in the regions with greater membrane curvature. Therefore, when $G \neq 0$, the membrane prefers to form many mountain-like regions with inclusions aggregating on them.

4.2 Simulation results

To focus on the mechanisms that we propose in our model clearly, two special cases with different interactions between the inclusions and lipids are studied in the simulations.

In case 1, $\tilde{J}_{02} = \tilde{J}_{12} \equiv \tilde{J}_0 + \tilde{J} > 0$, $\tilde{J}_{00} = \tilde{J}_{11} = \tilde{J}_{22} = \tilde{J}_{01} = \tilde{J}_0$, $G_1 = 0$, $G_2 \neq 0$, i.e., effectively excited state inclusions tend to attract with each other and induce local membrane curvature; ground state inclusions do not attract or repel with other

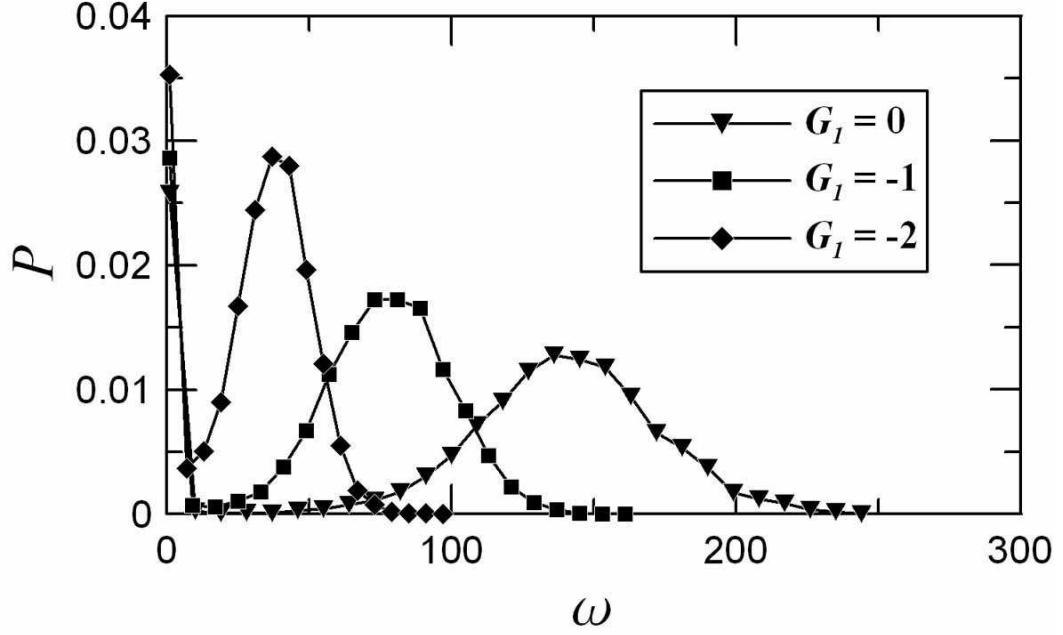


Figure 4.1: $P(\omega)$, the probability that an inclusion is found in a cluster with ω -patches, for $\kappa = 5 \times 10^{-20} N \cdot m$, $\gamma = 24 \times 10^{-6} N/m$, $\phi_{inc} = 12.5\%$, $K_{off}\Delta t = 10^{-3}$, $K_{on} = K_{off}/32$, $\tilde{J}_{01} = \tilde{J}_{12} = \tilde{J}_0 + 1.5$, all other $\tilde{J}_{mn} = \tilde{J}_0$, $G_2 = 0$, and $G_1 = 0$ (triangle-down), $G_1 = -1$ (square), $G_1 = -2$ (diamond). $P(\omega)$ has maximum at $\omega = 1$ comes from single-inclusion clusters spreading around in the “inclusion-poor” domains. Another maximum of $P(\omega)$ at greater M comes from finite-size inclusion clusters, this is the typical size of the inclusion clusters and it decreases as $|G_1|$ increases due to inclusion-curvature coupling.

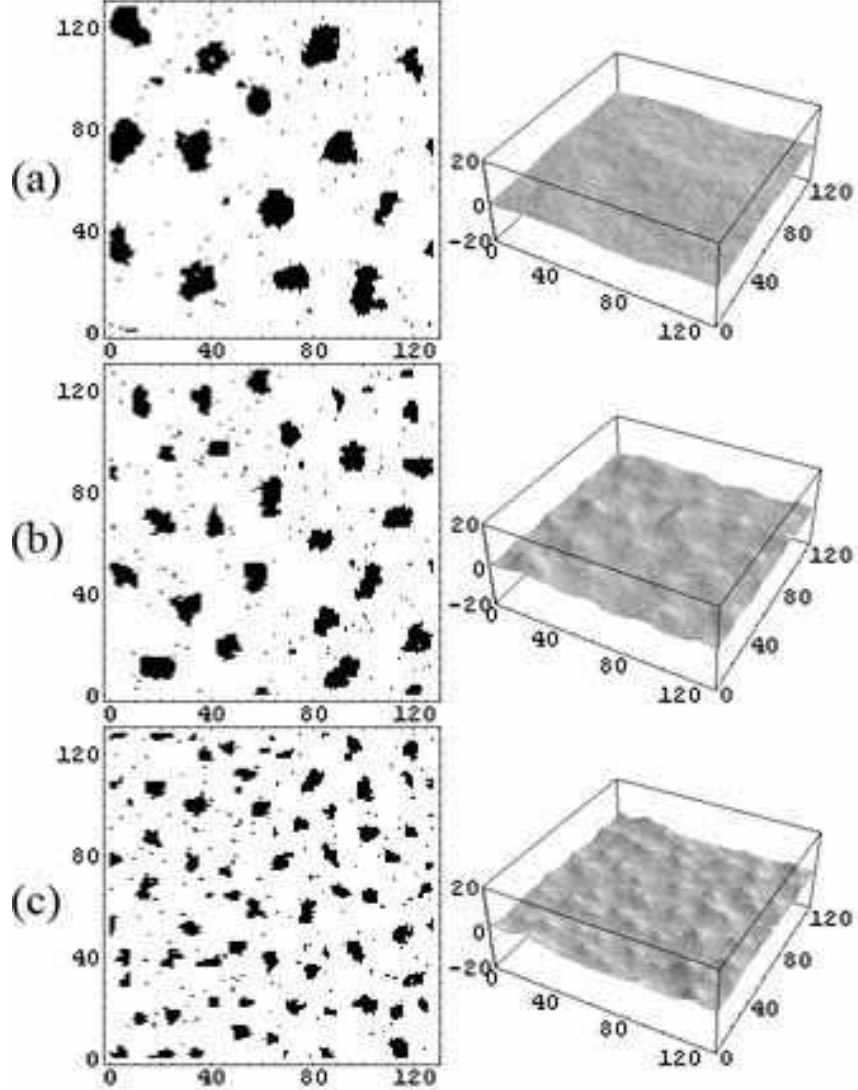


Figure 4.2: Typical snapshots for steady state inclusion distribution and membrane morphology for $\kappa = 5 \times 10^{-20} N \cdot m$, $\gamma = 24 \times 10^{-6} N/m$, $\phi_{inc} = 12.5\%$, $K_{off} \Delta t = 10^{-3}$, $K_{on} = K_{off}/32$, $\tilde{J}_{01} = \tilde{J}_{12} = \tilde{J}_0 + 1.5$, all other $\tilde{J}_{mn} = \tilde{J}_0$, and $G_2 = 0$. (a) $G_1 = 0$. (b) $G_1 = -1$. (c) $G_1 = -2$. As $|G_1|$ increases, the curvature of the membrane close to the inclusion-rich domains increases and the typical size of inclusion clusters becomes smaller. The length scale in the z -direction is chosen to be the same as x and y directions (the unit length is a) in order to faithfully present the morphology of the membrane.

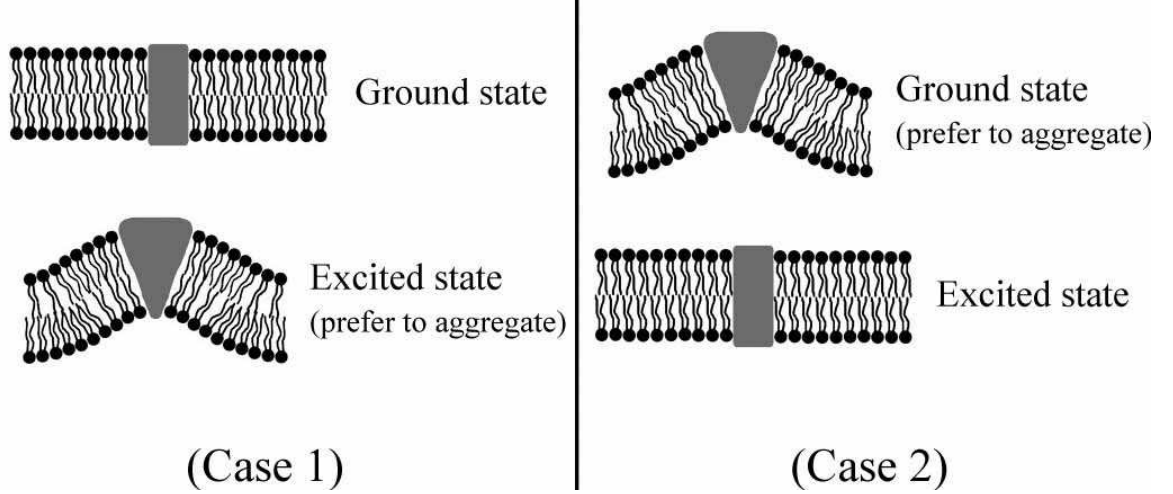


Figure 4.3: Schematics of inclusion conformation and inclusion-curvature coupling. In case 1, the excited state inclusions induce local membrane curvature, and the density of ground state inclusions is not coupled to local membrane curvature. In case 2, the ground state inclusions induce local membrane curvature, and the density of excited state inclusions is not coupled to local membrane curvature.

molecules, and the density of ground state inclusions is not coupled to local membrane curvature. In case 2, $\tilde{J}_{01} = \tilde{J}_{12} \equiv \tilde{J}_0 + \tilde{J} > 0$, $\tilde{J}_{00} = \tilde{J}_{11} = \tilde{J}_{22} = \tilde{J}_{02} = \tilde{J}_0$, $G_2 = 0$, $G_1 \neq 0$, i.e., effectively ground state inclusions tend to attract with each other and induce local membrane curvature; excited state inclusions do not attract or repel with other molecules, and the density of ground state inclusions is not coupled to local membrane curvature. Schematics of the conformations of inclusions are shown in Figure 4.3. We fix K_{off} , the relaxation rate of excited inclusions, and study the distribution of inclusions for different ϕ_{inc} , K_{on} , G_1 , and G_2 . All simulations are

carried out with $\kappa = 5 \times 10^{-20} N \cdot m$, $\gamma = 24 \times 10^{-6} N/m$, $a = 5nm$, $h_0 = 1nm$, and $\Delta t \approx 10^{-5} s$.

4.2.1 Short-time in-plane motions of inclusions

Although the main focus of this thesis is the size distribution of inclusion clusters, the effects of conformational change of the inclusions and inclusion-curvature coupling to the motion of the inclusions in the membrane are also of great interest. Therefore we begin our discussion with short-time in-plan motion of the inclusions. The mean square displacement $\langle d^2(t) \rangle$ of an inclusion in short time interval t for case 2 with $\phi_{inc} = 12.5\%$, $\tilde{J} = 1.5$, $K_{off}\Delta t = 10^{-3}$, and $K_{on} = K_{off}/128$ is illustrated in Figure 4.4. It is clear that $\langle d^2 \rangle \sim t$ at sufficiently large t , and the inclusions with greater inclusion-curvature coupling move slower in the membrane. Thus we define “effective diffusion constant” of an inclusion as the slope of the straight region of the $\langle d^2 \rangle - t$ curve. Figure 4.5 shows the relation between D_{eff} and K_{on} for case 1 with $\phi_{inc} = 12.5\%$, $\tilde{J} = 1.5$, and $K_{off}\Delta t = 10^{-4}$. It is clear that D_{eff} decreases when $|G_2|$ increases, but D_{eff} does not depend strongly on K_{on} . Figure 4.6 shows the relation between D_{eff} and K_{on} in case 2 with $\phi_{inc} = 12.5\%$, $\tilde{J} = 1.5$, and $K_{off}\Delta t = 10^{-3}$. It is clear that D_{eff} decreases when $|G_1|$ increases, too. Another interesting feature is that when $G_1 = -2$, D_{eff} shows strong dependence on K_{on} .

Figure 4.7 explains the strong dependence of D_{eff} on $|G|$. The free energy is lower when a curved inclusion stays in a curved region, and the free energy is higher when a curved inclusion stays in a flat region. Therefore it is less possible for this

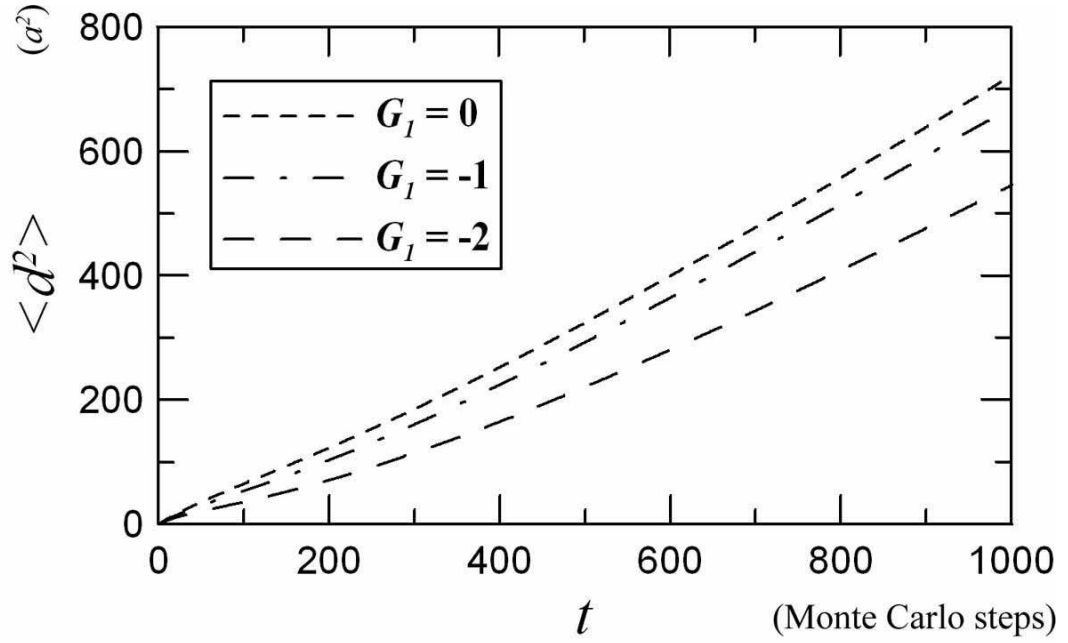


Figure 4.4: $\langle d^2 \rangle$ of an inclusion within short time interval t for case 2 with $\phi_{inc} = 12.5\%$, $\tilde{J} = 1.5$, $K_{off}\Delta t = 10^{-3}$, $K_{on} = K_{off}/128$, and $G_2 = 0$. $\langle d^2 \rangle \sim t$ at sufficiently large t , and the inclusions with stronger inclusion-curvature coupling move slower in the membrane.

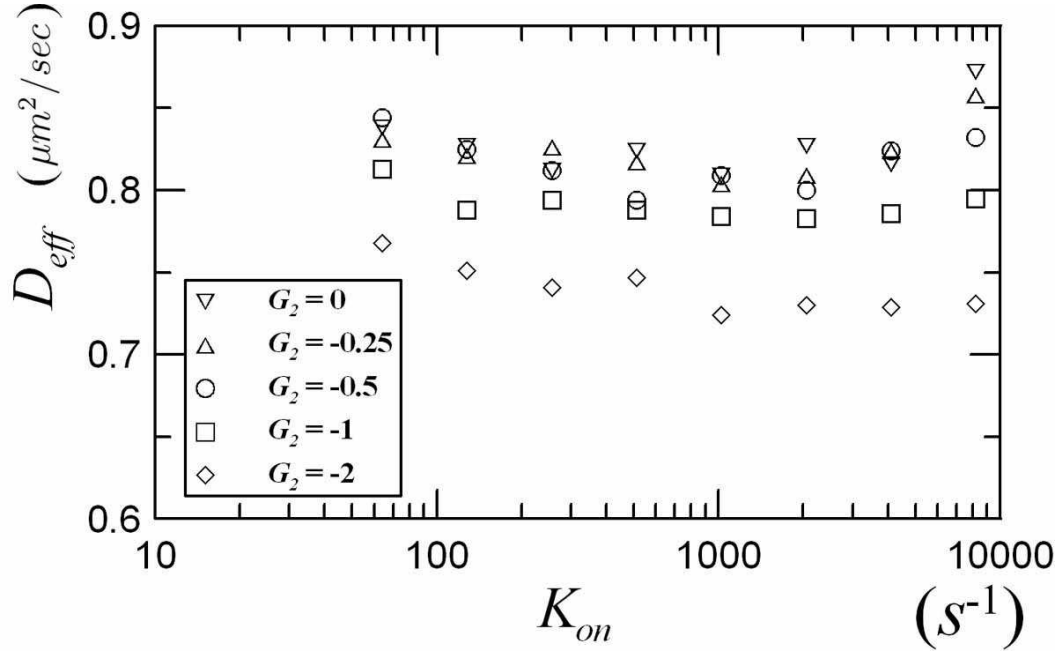


Figure 4.5: D_{eff} in case 1 with $\phi_{inc} = 12.5\%$, $\tilde{J} = 1.5$, $K_{off}\Delta t = 10^{-4}$, and $G_2 = 0$ (triangle-down), -0.25 (triangle-up), -0.5 (circle), -1 (square), and -2 (diamond). We can find that D_{eff} decreases as $|G_2|$ increases, but D_{eff} does not depend strongly on K_{on} . At large $|G_2|$, the tending is that D_{eff} first decreases as K_{on} increases, then the dependence becomes less significant at large K_{on} .

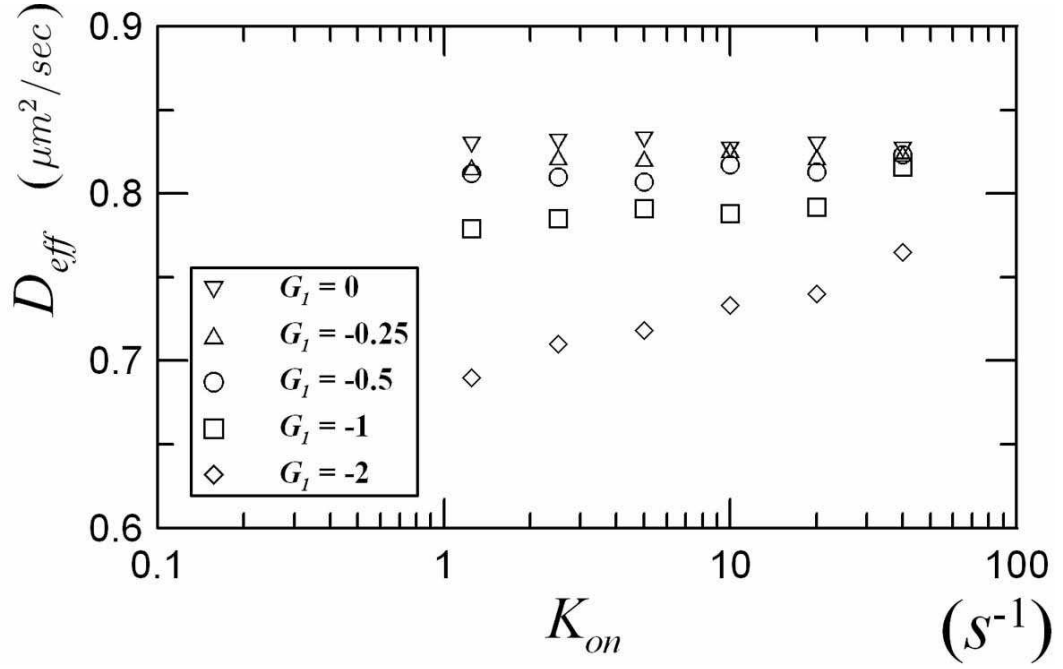


Figure 4.6: D_{eff} in case 2 with $\phi_{inc} = 12.5\%$, $\tilde{J} = 1.5$, $K_{off}\Delta t = 10^{-3}$, and $G_1 = 0$ (triangle-down), -0.25 (triangle-up), -0.5 (circle), -1 (square), and -2 (diamond). It is clear that D_{eff} decreases when $|G_2|$ increases. Another interesting feature is that when $G_1 = -2$, D_{eff} shows strong dependence on K_{on} .

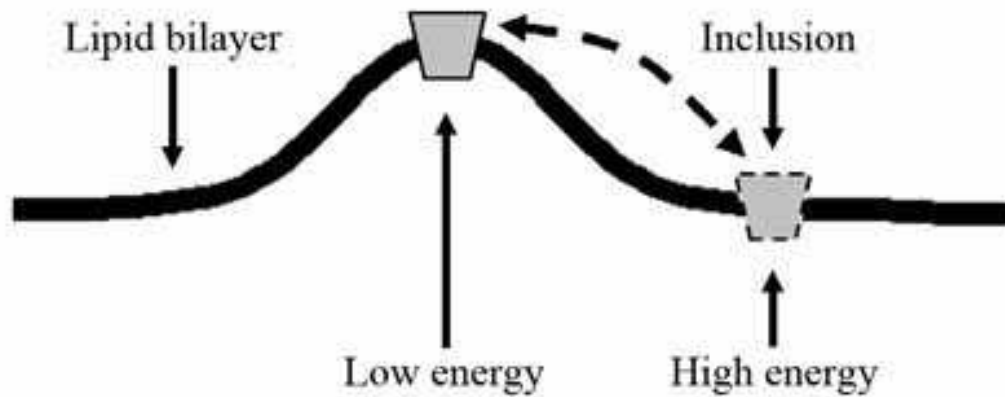


Figure 4.7: The strong dependence of D_{eff} on $|G|$ is explained in this figure. The free energy is lower when a curved inclusion stays in a curved region, and the free energy is higher when a curved inclusion stays in a flat region. Therefore it is less possible for this inclusion to move from a curved region to a flat region. When the inclusion-curvature coupling is stronger, this “caging” effect is more significant.

inclusion to move from a curved region to a flat region. When the inclusion-curvature coupling is stronger, this “caging” effect is more significant. This explains why large inclusion-curvature coupling results in small D_{eff} .

Moreover, in case 2, when K_{on} increases an inclusion spends less time in the ground state. Thus D_{eff} strongly depends on the K_{on} when $|G_1|$ is sufficiently large. On the other hand, in case 1 K_{off} is chosen to be such that $K_{on} > K_{off}$ for all K_{on} . Thus when K_{on} increases, an inclusion spends most of the time in the excited state if $K_{on} \gg K_{off}$. Thus at large $|G_2|$, the tendency is that D_{eff} first decreases as K_{on} increases, then the dependence becomes less significant at large K_{on} .

4.2.2 Case 1

In case 1, when $K_{off}\Delta t \gtrsim 10^{-3}$ (i.e., $K_{off} \gtrsim 10^2 s^{-1}$, characteristic time scale of a cycle of a motor protein), no inclusion clusters are observed in simulations for $K_{on} \lesssim 10^3 s^{-1}$. This indicates that in a system with typical inclusion excitation and relaxation rates, activities may completely suppress the formation of inclusion clusters. This is because when K_{off} is sufficiently large, the lifetime of excited state inclusions is sufficiently short such that the excited-state inclusions does not have time to aggregate. For $K_{off}\Delta t = 10^{-4}$ (i.e., $K_{off} \sim 10 s^{-1}$, this is more likely for the case when the relaxation of an inclusion is induced by ligands), inclusion clusters are observed for a wide range of K_{on} .

Figure 4.8 shows the snapshots of the distribution of inclusions in the membrane for case 1 with $\phi_{inc} = 12.5\%$, $\tilde{J} = 1.5$, and $K_{off}\Delta t = 10^{-4}$ on a 128×128 square

lattice. The typical size of inclusion clusters increases as K_{on} increases or $|G_2|$ decreases. Moreover, the dependence of the typical size of inclusion clusters on the value of K_{on} is more evident for small $|G_2|$. Figure 4.9 shows the relation between \sqrt{M} and $K_{on}\Delta t$ for $K_{off}\Delta t = 10^{-4}$ on a 128×128 square lattice. In Figure 4.9 (a) $\phi_{inc} = 12.5\%$, $\tilde{J} = 1.5$; in Figure 4.9 (b) $\phi_{inc} = 25\%$, $\tilde{J} = 1$. The only exception is the empty symbol with the greatest value of \sqrt{M} in Figure 4.9 (b), which is taken from simulations performed on a 256×256 square lattice. The filled symbols denote the situation when $K_{on}\Delta t = 1$, the maximum excitation rate can be simulated in our simulations.

Both Figure 4.9 (a) and (b) indicate that when G_2 is small, \sqrt{M} shows weak dependence on $K_{on}\Delta t$ for a wide range of $K_{on}\Delta t$, but increases fast when $K_{on}\Delta t \gtrsim 0.01$. This can be understood by comparing the diffusion length of a ground state inclusion within its lifetime and the typical size of inclusion clusters. Because the diffusion distance during the lifetime of a ground state inclusion is $\approx \sqrt{4D_{eff}K_{on}^{-1}}$. Therefore when $\sqrt{4D_{eff}K_{on}^{-1}} \lesssim \sqrt{M}$, more and more ground state inclusions can not escape from an inclusion cluster as K_{on} increases. This “positive feedback” of K_{on} dependence of \sqrt{M} is responsible for the strong K_{on} dependence of \sqrt{M} at large K_{on} . From the discussion of the previous subsection, $D_{eff} \approx 0.8\mu m^2/sec \approx 0.8a^2/\Delta t$, then the critical length scale is $\sqrt{4D_{eff}K_{on}^{-1}} \approx K_{on}^{-1/2}$. Therefore, \sqrt{M} increases fast at $K_{on}\Delta t \gtrsim 0.01$ ($\sqrt{M} \approx 10$) in case 1.

Another important feature of Figure 4.9 is that for the filled symbols with $G_2 = 0$, in Figure 4.9 (a) $\sqrt{N_{inc}} \approx \sqrt{M} \approx 45$; in Figure 4.9 (b) $\sqrt{N_{inc}} = 64$ and $\sqrt{M} \approx 60$, i.e., almost all inclusions aggregate in the same inclusion cluster .

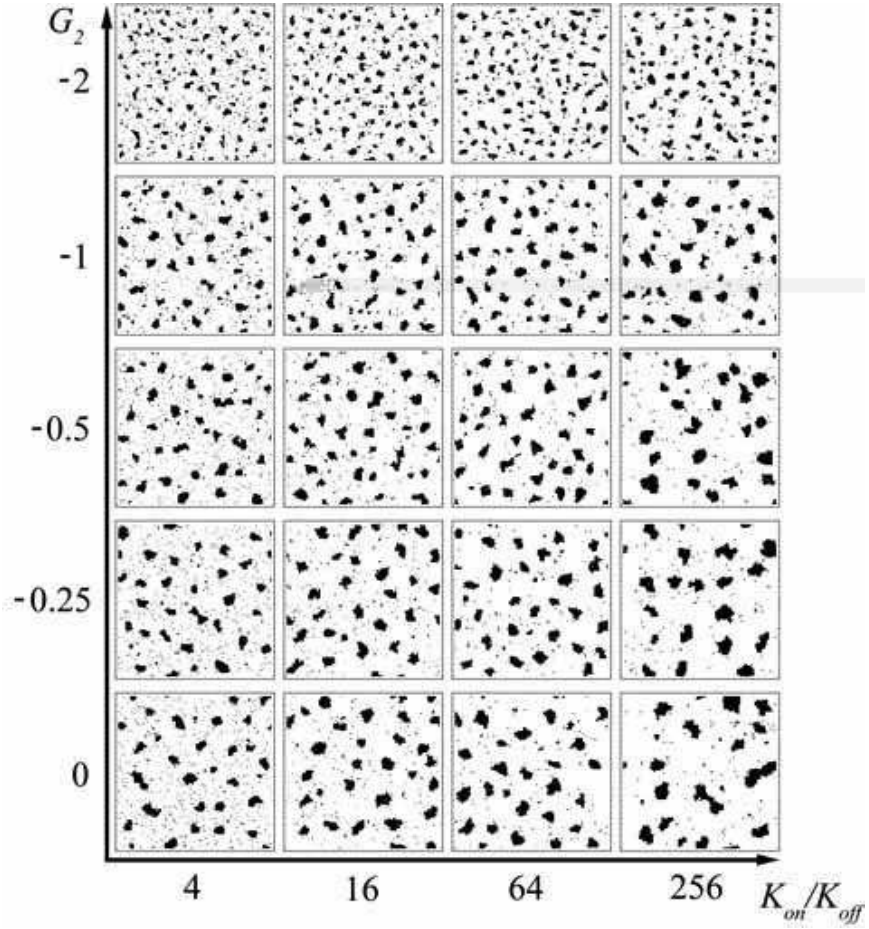


Figure 4.8: The distribution of inclusions in the membrane for case 1 with $\phi_{inc} = 12.5\%$, $\tilde{J} = 1.5$, and $K_{off}\Delta t = 10^{-4}$. The typical length scale of inclusion clusters increases as K_{on} increases or $|G_2|$ decreases. Moreover, the typical size of inclusion clusters increases faster when $|G_2|$ is smaller.

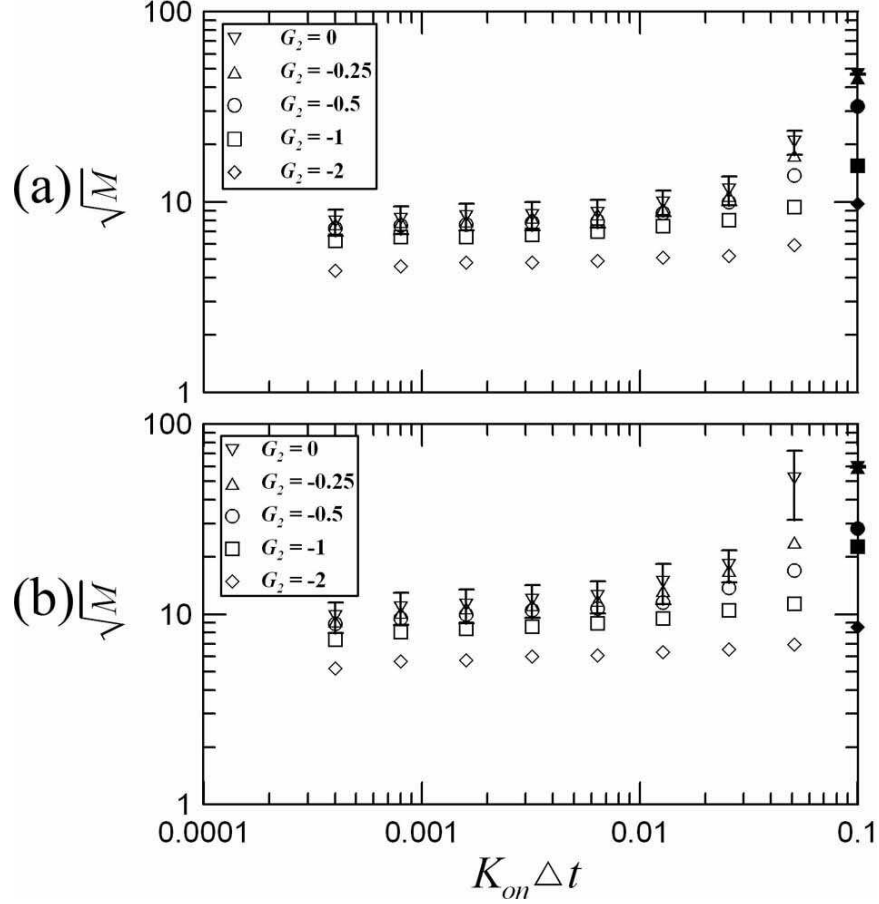


Figure 4.9: This relation between \sqrt{M} and K_{on} in case 1 for $K_{off}\Delta t = 10^{-4}$, $G_2 = 0$ (triangle-down), -0.25 (triangle-up), -0.5 (circle), -1 (square), and -2 (diamond), (a): $\phi_{inc} = 12.5\%$, $\tilde{J} = 1.5$; (b): $\phi_{inc} = 25\%$, $\tilde{J} = 1$. The filled symbols denote the situation when $K_{on}\Delta t = 1$, the maximum excitation rate can be simulated in the simulations, the error bar in this situation is smaller than the symbol. When the inclusion-curvature coupling is small, \sqrt{M} shows weak dependence on $K_{on}\Delta t$ for a wide range of $K_{on}\Delta t$, but increases fast when $K_{on}\Delta t \gtrsim 0.01$. Furthermore, the coupling between inclusion density and membrane curvature provides the upper limit of the typical size of the inclusion clusters, and suppresses the formation of large inclusion clusters.

Moreover, when $G_2 \neq 0$, \sqrt{M} decreases as $|G_2|$ increases. This indicates that even when all inclusions are all in the excited state, the coupling between inclusion density and membrane curvature provides the upper limit of the typical size of the inclusion clusters, and suppresses the formation of large inclusion clusters. This is because the system has lower free energy when the inclusions locate in the regions with greater membrane curvature. Therefore, the membrane prefers to form many mountain-like regions with inclusions aggregating on them, when $G \neq 0$.

4.2.3 Case 2

In case 2, inclusion clusters have been observed for $K_{off}\Delta t = 10^{-2} - 10^{-3}$, and a wide range of K_{on} . All simulations are performed on a 128×128 square lattice in case 2.

Figure 4.10 shows the snapshots of the distribution of inclusions in the membrane for case 2 with $\phi_{inc} = 12.5\%$, $\tilde{J} = 1.5$, and $K_{off}\Delta t = 10^{-3}$. The typical size of inclusion clusters decreases as K_{on} increases or $|G_1|$ increases. Moreover, the dependence of the typical size of inclusion clusters on the value of K_{on} is more evident for small $|G_1|$. Figure 4.11 shows the relation between \sqrt{M} and $K_{on}\Delta t$. In Figure 4.11 (a) $\phi_{inc} = 12.5\%$, $\tilde{J} = 1.5$, and $K_{off}\Delta t = 10^{-3}$, in Figure 4.11 (b) $\phi_{inc} = 25\%$, $\tilde{J} = 1$, and $K_{off}\Delta t = 10^{-3}$, in Figure 4.11 (c) $\phi_{inc} = 12.5\%$, $\tilde{J} = 1.5$, and $K_{off}\Delta t = 10^{-2}$. The filled symbols denote the situation when all inclusions are in the ground state, i.e., $K_{on} = 0$.

When the density of the inclusions is not coupled to local membrane curvature, it agrees with $\sqrt{M} \sim K_{on}^{-\frac{1}{3}}$ relation pretty well for a wide range of K_{on} . This is

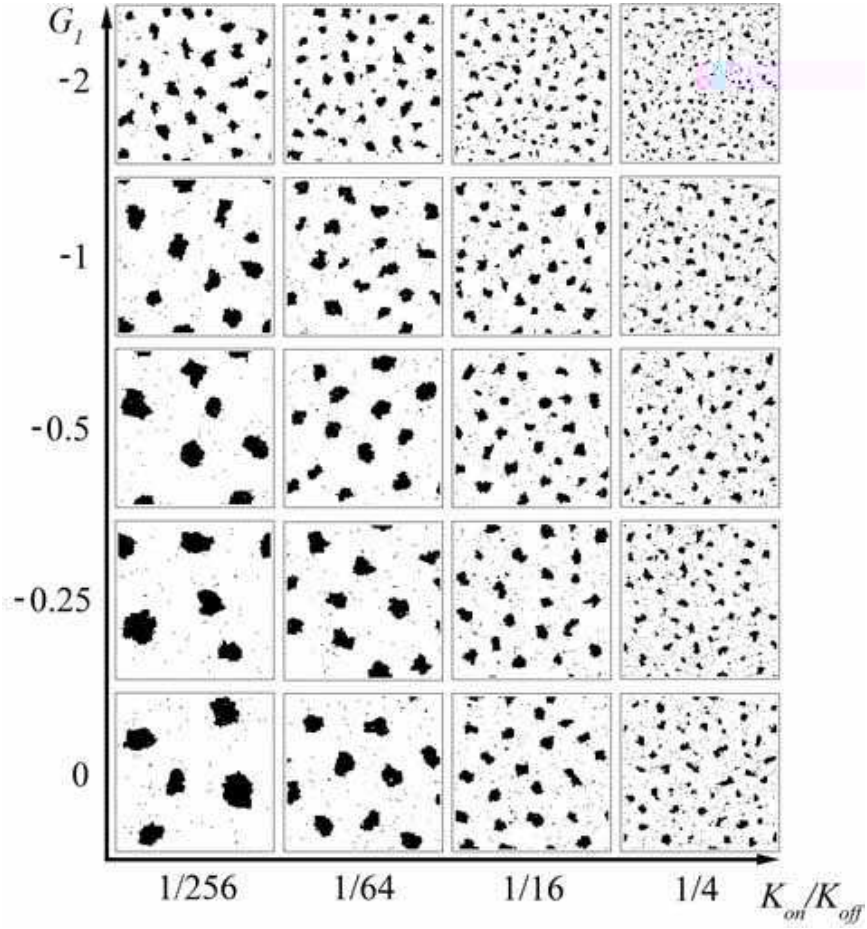


Figure 4.10: The distribution of inclusions in the membrane for case 2 with $\phi_{inc} = 12.5\%$, $K_{off}\Delta t = 10^{-3}$, and $\tilde{J} = 1.5$. The typical length scale of inclusion cluster increases as K_{on} decreases or $|G_1|$ decreases. Moreover, the typical size of inclusion clusters increases faster when $|G_1|$ is smaller.

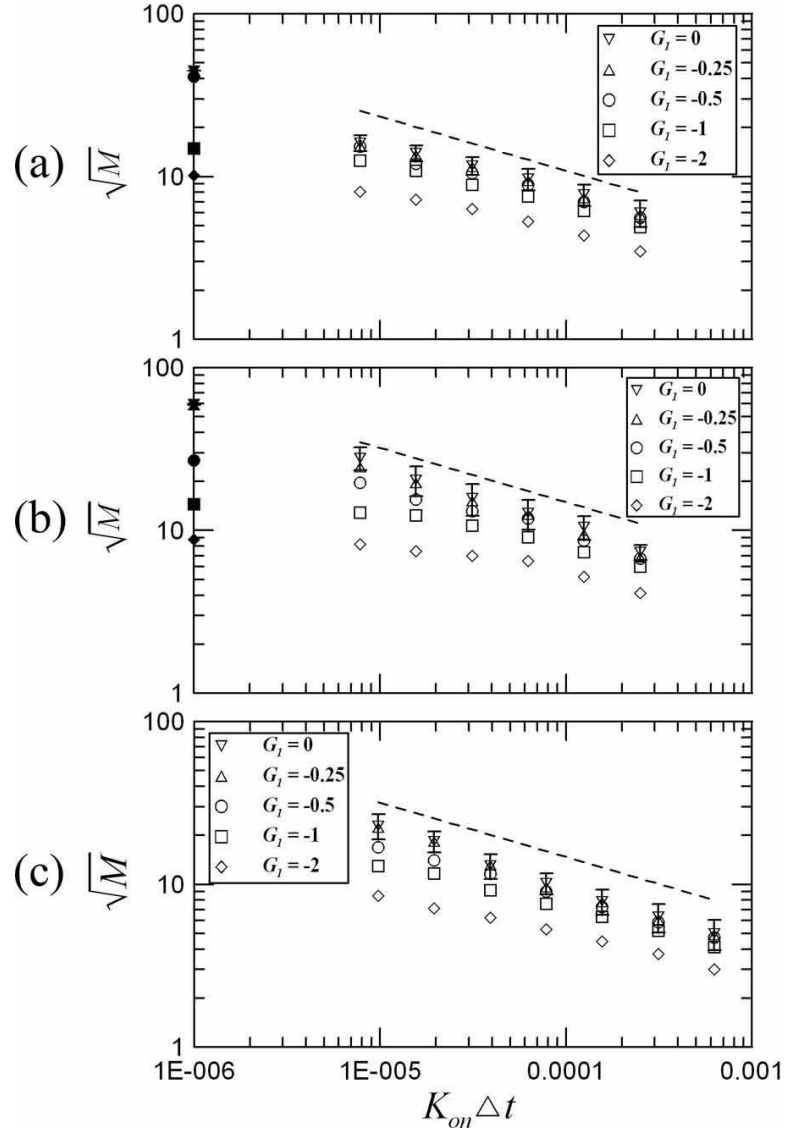


Figure 4.11: The relation between \sqrt{M} and K_{on} in case 1 for (a): $\phi_{inc} = 12.5\%$, $\tilde{J} = 1.5$, and $K_{off}\Delta t = 10^{-3}$; (b): $\phi_{inc} = 25\%$, $\tilde{J} = 1$, and $K_{off}\Delta t = 10^{-3}$; (c): $\phi_{inc} = 12.5\%$, $\tilde{J} = 1.5$, $K_{off}\Delta t = 10^{-2}$. The filled symbols denote the situation when all inclusions are in the ground state, and $K_{on} = 0$, and the error bar in this situation is smaller than the symbol. $G_1 = 0$ case agrees with $\sqrt{M} \sim K_{on}^{-\frac{1}{3}}$ relation pretty well for a wide range of K_{on} . The slope of the dotted line is $-\frac{1}{3}$.

because when there is no budding in the membrane, the growth of inclusion clusters in the absence of inclusion activities and inclusion-curvature coupling corresponds to a two-dimensional phase separation dynamics, i.e., $\sqrt{M} \sim t^{1/3}$. [16, 17] This growth eventually saturates due to the active transitions of the inclusions. Since the lifetime of ground state inclusions is K_{on}^{-1} , thus the typical length scales of inclusion clusters in the steady state should obey $\sqrt{M} \sim K_{on}^{-1/3}$. [8]

The same as case 1, for the filled symbol with $G_1 = 0$, almost all inclusions aggregate in the same inclusion cluster (in Figure 4.11 (a) $\sqrt{N_{inc}} \approx \sqrt{M} \approx 45$; in Figure 4.11 (b) $\sqrt{N_{inc}} = 64$ and $\sqrt{M} \approx 60$). Moreover, when $G_1 \neq 0$, \sqrt{M} decreases as $|G_1|$ increases. Therefore, the coupling between inclusion density and membrane curvature provides the upper limit of the typical size of the inclusion clusters, and suppresses the formation of large inclusion clusters as in case 1.

Notice that Figure 4.11 (a) and (b) have different ϕ_{inc} and different J_{mn} , but at the same K_{on} the typical length scales of inclusion clusters are almost in the same range. Furthermore, K_{off} in (c) is tenfold of K_{off} in (a), but at the same K_{on} the typical length scales of inclusion clusters are also almost in the same range. This means that K_{on} is the key factor controls the size of inclusion clusters.

In case 2 the lifetime of the state that prefers to aggregate is changed when K_{on} is changed, but in case 1 the lifetime of the state that prefers to leave the inclusion clusters is changed when K_{on} is changed. Therefore, case 1 and case 2 are different, and this is the reason why the K_{on} dependence in these two cases are so different.

Chapter 5

Summary

Our Monte Carlo simulations on a simple toy model have shown that inclusion activities and inclusion-curvature coupling both could contribute to the formation of finite-size inclusion clusters in biological membranes. Since the inclusions have two internal states, and the conformational changes of the inclusions are induced by external stimuli. Thus, we treat a biomembrane as an active, nonequilibrium system. Two special cases with different interactions between the inclusions and lipids are studied in the simulation. In case 1, excited state inclusions attract with each other and induce local membrane curvature; ground state inclusions do not attract or repel with other molecules, and the density of ground state inclusions is not coupled to local membrane curvature. In case 2, ground state inclusions tend to attract with each other and induce local membrane curvature; excited state inclusions do not attract or repel with other molecules, and the density of excited state inclusions is not coupled to local membrane curvature. Our main results are:

- (1) The effective diffusion constant of the inclusions decreases as the inclusion-

curvature coupling and the lifetime of the state with inclusion-curvature coupling increases.

(2) In case 1, we find that when K_{off} is sufficiently large, the excited-state inclusions does not have time to aggregate, and there is no inclusion cluster in the system for a wide range of K_{on} .

(3) In case 1, when inclusion-clusters do form, typical size of clusters shows weak dependence on the excitation rate of the inclusions for a wide range of K_{on} , but increases fast when K_{on} is greater than some critical value. Because the diffusion distance of a ground state inclusion in the inclusion cluster $\sim \sqrt{4D_{eff}K_{on}^{-1}} \sim K_{on}^{-1/2}$. When $\sqrt{M} \gtrsim K_{on}^{-1/2}$ the inclusions become hard to escape from an inclusion cluster.

(4) In case 2, we find that when the density of the inclusions is not coupled to local membrane curvature, it agrees with $\sqrt{M} \sim K_{on}^{-\frac{1}{3}}$ relation pretty well for a wide range of K_{on} . This is because when there is no budding in the membrane, the growth of inclusion clusters in the absence of inclusion activities and inclusion-curvature coupling corresponds to a two-dimensional phase separation dynamics, i.e., $\sqrt{M} \sim t^{1/3}$. This growth eventually saturates at time scale $\sim K_{on}^{-1}$ due to the active transitions of the inclusions.

(5) Moreover, in both case 1 and case 2, we find that the coupling between inclusion density and membrane curvature provides the upper limit of the typical size of the inclusion clusters, and suppresses the formation of large inclusion clusters.

Our simple model has neglected many complications that occur in real biological membrane. For example: (i) We ignored the effect of cytoskeleton on the motion of the inclusions. [18] (ii) The effect of solution flow is not incorporated in our model. [19] (iii)

Our model is not appropriate to describe budding in biomembrane. [20] New models that includes the aforementioned mechanisms will be our future research direction.

APPENDICES

Appendix A

Non-dimensionalization of the Hamiltonian

The Hamiltonian of the membrane can be written as

$$\begin{aligned} H_{lattice} = & \sum_{(i,j)} \frac{a^2}{2} \left[\kappa (\nabla_{\perp}^2 h)_{ij}^2 + \gamma (|\nabla_{\perp} h|^2)_{ij} \right] \\ & - \sum_{(i,j)} \sum_{p=0}^2 a^2 \kappa C_p \phi_p(i,j) (\nabla_{\perp}^2 h)_{ij} \\ & + \frac{1}{2} \sum_{\langle\langle i,j \rangle\rangle \langle\langle k,l \rangle\rangle} \left(\sum_{m,n} J_{mn} \phi_m(i,j) \phi_n(k,l) \right). \end{aligned} \quad (\text{A.1})$$

First, we choose the unit of energy to be $k_B T$. Then we choose the unit length of local vertical height of membrane to be $h_0 \sim \frac{a\sqrt{k_B T}}{\sqrt{\kappa}}$. Thus the first term of $H_{lattice}$ at $h \sim h_0$, $\nabla_{\perp}^2 \sim \frac{1}{a^2}$ is on the order of $k_B T$. The discretized Laplacian and gradient of

h in two dimension are

$$\begin{aligned}
\nabla_{\perp}^2 h &= \frac{\partial^2 h}{\partial x^2} + \frac{\partial^2 h}{\partial y^2} \\
&= \frac{\partial}{\partial x} \left(\frac{h_{x+\frac{a}{2},y} - h_{x-\frac{a}{2},y}}{a} \right) + \frac{\partial}{\partial y} \left(\frac{h_{x,y+\frac{a}{2}} - h_{x,y-\frac{a}{2}}}{a} \right) \\
&= \frac{1}{a^2} (h_{x+a,y} + h_{x-a,y} + h_{x,y+a} + h_{x,y-a} - 4h_{x,y}) \\
&= \frac{a}{a^2} \sqrt{\frac{k_B T}{\kappa}} \left(\tilde{h}_{i+1,j} + \tilde{h}_{i-1,j} + \tilde{h}_{i,j+1} + \tilde{h}_{i,j-1} - 4\tilde{h}_{i,j} \right) \\
&\equiv \frac{1}{a} \sqrt{\frac{k_B T}{\kappa}} \tilde{\nabla}_{\perp}^2 \tilde{h},
\end{aligned} \tag{A.2}$$

and

$$\begin{aligned}
\nabla_{\perp} h &= \frac{\partial h}{\partial x} \hat{i} + \frac{\partial h}{\partial y} \hat{j} \\
&= \frac{1}{2a} \left[(h_{x+a,y} - h_{x-a,y}) \hat{i} + (h_{x,y+a} - h_{x,y-a}) \hat{j} \right] \\
&= \frac{a}{2a} \sqrt{\frac{k_B T}{\kappa}} \left[(\tilde{h}_{i+1,j} - \tilde{h}_{i-1,j}) \hat{i} + (\tilde{h}_{i,j+1} - \tilde{h}_{i,j-1}) \hat{j} \right] \\
&\equiv \sqrt{\frac{k_B T}{\kappa}} \tilde{\nabla}_{\perp} \tilde{h}.
\end{aligned} \tag{A.3}$$

Thus, total Hamiltonian becomes

$$\begin{aligned}
k_B T \tilde{H}_{lattice} &= \sum_{(i,j)} \frac{a^2}{2} \left[\kappa \frac{k_B T}{a^2 \kappa} (\tilde{\nabla}_{\perp}^2 \tilde{h})_{ij}^2 + \gamma \frac{k_B T}{\kappa} \left(|\tilde{\nabla}_{\perp} \tilde{h}|^2 \right)_{ij} \right] \\
&\quad - \sum_{(i,j)} \sum_{p=0}^2 a^2 \kappa C_p \phi_p(i,j) \frac{\sqrt{k_B T}}{a \sqrt{\kappa}} (\tilde{\nabla}_{\perp}^2 \tilde{h})_{ij} \\
&\quad + \frac{1}{2} \sum_{\langle (i,j)(k,l) \rangle} \left(\sum_{m,n} k_B T \tilde{J}_{mn} \phi_m(i,j) \phi_n(k,l) \right).
\end{aligned} \tag{A.4}$$

From the definition of dimensionless of inclusion-curvature coupling $G_i \equiv h_0 C_i$, we can obtain the non-dimensionalized Hamiltonian of the system

$$\begin{aligned}
\tilde{H}_{lattice} = & \sum_{(i,j)} \frac{1}{2} \left[\left(\tilde{\nabla}_{\perp}^2 \tilde{h} \right)_{ij}^2 + \frac{\gamma a^2}{\kappa} \left(\left| \tilde{\nabla}_{\perp} \tilde{h} \right|^2 \right)_{ij} \right] \\
& - \sum_{(i,j)} \sum_{p=0}^2 G_p \phi_p(i, j) \left(\tilde{\nabla}_{\perp}^2 \tilde{h} \right)_{ij} \\
& + \frac{1}{2} \sum_{\langle\langle i,j \rangle\rangle \langle\langle k,l \rangle\rangle} \left(\sum_{m,n} \tilde{J}_{mn} \phi_m(i, j) \phi_n(k, l) \right). \tag{A.5}
\end{aligned}$$

BIBLIOGRAPHY

Bibliography

- [1] H. Lodish et al., *Molecular cell biology*, 3rd ed (W.H. Freeman, New York, 1995).
- [2] G. Vereb et al, Proc. Natl. Acad. Sci. USA **100**, 8053, (2003).
- [3] S.L. Veatch, I.V. Polozov, K. Gawrisch, and S.L. Keller, Biophys. J. **86**, 2910, (2004).
- [4] M.S. Turner, P. Sens, and N.D. Socci, Phys. Rev. Lett. **95**, 168301, (2005).
- [5] L. Forest, Europhys. Lett. **71**, 508, (2005).
- [6] K. Simons and E. Ikonon, Nature, **387**, 569, (1997).
- [7] E. Sparr, Langmuir **15**, 6950, (1999).
- [8] H.Y. Chen, Phys. Rev. Lett. **92**, 16, (2004).
- [9] T.R. Weikl, Phys. Rev. E **66**, 061915, (2002).
- [10] M.C. Sabra and O.G. Mouritsen, Biophys. J. **74**, 745, (1998).
- [11] H. Strey, M. Peterson, and E. Sackmann, Biophys. J. **69**, 478, (1995).
- [12] Needham. D. and R. M. Hochmuth, Biophys. J. **61**, 1664, (1992).

- [13] K. Binder and D.W. Heermann, *Monte Carlo Simulation in Statistical Physics*.
2nd corrected ed. (Springer-Verlag, Berlin, 1992).
- [14] W.R. Gibbs, *Computation in Modern Physics*. (World Scientific, Singapore,
1994).
- [15] T.R. Weikl and R. Lipowsky, *Biophys. J.* **87**, 3665, (2004).
- [16] M. Seul, N. Y. Morgan, and C. Sire, *Phys. Rev. Lett.* **73**, 2284, (1994).
- [17] A. J. Bray, *Adv. Phys.* **43**, 357, (1994).
- [18] L. C. -L Lin and F. L. H. Brown, *Biophys. J.* **86**, 764, (2004).
- [19] M. Doi and S. F. Edwards, *The Theory of Polymer Dynamics*. (Clarendon Press,
Oxford, 1993).
- [20] H-G Döbereiner, E. Evanc, U. Seifert, and M. Wartis, *Phys. Rev. Lett.* **75**, 3360,
(1995).